AIAA JOURNAL
Vol. 57, No. 9, September 2019

Surface-Pressure-Based Estimation of the Velocity Field in a Separation Bubble

Burak A. Tuna,* John W. Kurelek,† and Serhiy Yarusevych‡
University of Waterloo, Waterloo, Ontario N2L 3G1, Canada

DOI: 10.2514/1.J058026

The effectiveness in estimating the velocity field in a laminar separation bubble using surface-pressure-based stochastic estimation methods is examined. A separation bubble is formed over a NACA 0018 airfoil at a Reynolds number of 125,000 and an angle of attack of 4°, while the velocity field and surface pressure fluctuations are measured simultaneously. Single-time-delay and multi-time-delay estimation techniques, in both single-point and multipoint formulations, are employed and compared, showing that the accuracy of the estimates increases notably through the inclusions of additional predictor events in both space and time. The multipoint, multi-time-delay estimation technique is shown to produce the most accurate estimates, with the reconstructed velocity fields capturing all essential flow features across the scales of interest. The accuracy of the estimates is shown to depend on location within the bubble, with the best results found in the region of the mean maximum bubble height, whereas performance decreases near the mean separation point. The latter is due to the transition to turbulence increasing the randomness of fluctuations and can be mitigated through more advanced stochastic estimation, whereas the former is a result of low disturbance amplitudes that fall within the noise level of the measurements.

Nomenclature

A	=	linear estimation coefficient
B	=	quadratic estimation coefficient
c	=	airfoil chord length
cov	=	covariance
f	=	frequency
f_{shed}	=	vortex shedding frequency
K	=	number of pressure sensors
l	=	airfoil surface arc length
N	=	number of realizations in time
N_d	=	number of time delays in multi-time-delay approach
N_v	=	number of vortices detected
n	=	number of points in the flow field
P'	=	fluctuating surface pressure event vector
p'	=	fluctuating surface pressure
t	=	time
t^*	=	dimensionless time; t/f_{shed}
u', v'	=	streamwise and wall-normal velocity fluctuations
x, y, z	=	streamwise, wall-normal, and spanwise directions
x_H	=	location of mean maximum bubble height
x_R	=	mean reattachment point
x_S	=	mean separation point
α	=	angle of attack
δ^*	=	displacement thickness
Γ_1	=	vortex identification criterion [56]
κ	=	fluctuating velocity magnitude ratio metric
λ_2	=	vortex identification criterion [55]
ρ	=	cross-correlation coefficient
σ	=	standard deviation
τ	=	time delay between conditional and unconditional events
$\Phi_{p'p'}$	=	spectra of surface pressure fluctuations
$\Phi_{v'v'}$	=	spectra of wall-normal velocity fluctuations
Ψ'	=	fluctuating velocity component field
$\tilde{\Psi}'$	=	estimated fluctuating velocity component field
Ω_z	=	spanwise vorticity

Received 21 October 2018; revision received 3 March 2019; accepted for publication 5 June 2019; published online 19 July 2019.

*Postdoctoral Research Associate, Mechanical & Mechatronics Engineering. Professional Member AIAA.

†Graduate Student, Mechanical & Mechatronics Engineering. Student Member AIAA.

‡Associate Professor, Mechanical & Mechatronics Engineering. Associate Fellow AIAA.

I. Introduction

STOCHASTIC estimation (SE), first introduced to fluid dynamics by Adrian [1,2], has been applied to numerous fluid flows, including turbulent boundary layers [3,4], shear layers [5–7], separating–reattaching flows [8–10], cavity flows [11–18], jets [19,20], and wake flows [21–26]. This technique allows for the analysis of turbulent flows through the identification of coherent structures from sparse conditional events. Adrian [27] showed that conditional averages of turbulent flow quantities can be approximated in terms of unconditional correlation data using SE. In the SE, the conditional averages are approximated through a Taylor expansion around the average value of the conditional event, which may be, for example, single-point (SP) or multipoint (MP) measurements of pressure from embedded surface pressure sensors [4].

The value in using SE lies in its ability to reconstruct velocity fields and thus obtain a global estimation of the spatial and temporal evolution of the coherent features in the flow field from uncorrelated velocity field measurements. The signals from a small number of fixed sensors within the flow domain, that is, those measuring surface pressure, are used to synchronize the coherent contributions and thus estimate the coherent flow field, with only a small number of fixed sensors required. This method can lead to an estimator for a given configuration, determined in a laboratory setting, which can then be employed in an analogous industrial application to estimate the flow field using only pointwise measurements, where entire flow field measurements are often not possible.

As a tool to estimate coherent velocity fluctuations, several SE methodologies have been developed, such as the SP and MP approaches. In the early applications by Adrian [2] and Cole et al. [19], measurements at one location were used, with the results demonstrating that such measurements are not sufficient to adequately estimate instantaneous velocity fields. Gieseke and Guezennec [21] improved the technique by employing MP pressure events, where the estimate of the velocity field was found by minimizing the root-mean-square (RMS) error between the estimated and input fields. They showed that higher levels of turbulent kinetic energy (TKE) could be recovered compared with the SP pressure events, thus producing a more representative estimate of the flow field using the MP SE method. In their simplest implementation, SP

and MP stochastic methods use conditional events from the same time instant at which the estimate is desired, which is referred to as the single-time-delay (STD) approach. The main drawback of this method arises when conditional and unconditional events are separated by a time lag, commonly due to a mean convective component in the velocity field. Some investigators have used a known time offset in their SE formulation [4,28] to address this problem for the single-time-delay approach; however, such a time lag must be known a priori. A multi-time-delay (MTD) approach has been suggested as an alternative method, which can be employed in the frequency domain [6,29] or in the time domain [16,30]. For the latter, past and current events are used in the SE formulation, which Ukeiley et al. [16] and Caraballo et al. [30] found successfully captured the dynamics of unsteady flow features and significantly improved the accuracy of the estimates over the STD approach.

The described SE methods have been applied in two formulations, namely, linear stochastic estimation (LSE) [5] and quadratic stochastic estimation (QSE) [4]. LSE retains the first-order terms in the Taylor series expansion, whereas the QSE method also retains the second-order terms. Naguib et al. [4] reported that the inclusion of the second-order terms leads to an improved estimation of the velocity field. Moreover, Murray and Ukeiley [13] employed both LSE and QSE in the case of a cavity flow, finding that the RMS velocity and TKE were better estimated by QSE. Similarly, Kastner et al. [31] reported that more representative levels of TKE in an axisymmetric jet flow were recovered by QSE.

The present investigation is focused on the assessment of the discussed SE methods applied to estimate salient flow dynamics in a laminar separation bubble using surface pressure measurements as conditional events. Laminar separation bubbles commonly form on lifting surfaces operating at aerodynamically low Reynolds numbers [32–34]. In such conditions, laminar boundary-layer separation takes place on the suction side, and the consequent laminar-to-turbulent transition in the separated shear layer leads to mean flow reattachment, hence forming a time-averaged separation bubble. Recent investigations have demonstrated that the overall flow development is dominated by the development of coherent structures during the later stages of transition [35–37]. To enhance performance, different active flow control strategies have been shown to be effective in controlling separation bubble parameters through influence over the coherent structures [38–43]. Thus, SE can offer valuable utility for flow diagnostics and control applications in separation bubbles; however, this has yet to be demonstrated in the literature. In this paper, the implementation and performance of different SE approaches applied to a separation bubble flow are considered, with the results providing a quantitative comparison of SP and MP, STD and MTD, and linear and quadratic SE techniques.

II. Mathematical Description of SE Approaches

SE techniques for the velocity field considered in the present investigation are briefly discussed here, with more detailed overviews available in [9,12,28,44]. The formulations discussed herein employ a generic variable $\Psi'(x, y; t)$, which represents any fluctuating velocity component in the flow field. In applying SE, it is assumed that $\Psi'(x, y; t)$, corresponding to an unconditional event P' (fluctuating surface pressure in the present investigation), is equivalent to the conditional average:

$$\tilde{\Psi}'(x, y; t) = \langle \Psi'(x, y; t) | P'_i(t) \rangle \tag{1}$$

where $\langle | \rangle$ is a conditional average operator. If the quantities $\Psi'(x, y; t)$ and $P'(t)$ have zero mean in time and are continuous, estimation of $\tilde{\Psi}'$ can be written as [2]:

$$\tilde{\Psi}'(x, y; t) = \sum_{i=1}^{K} A_i(x, y) P'_i(t) + \sum_{i=1}^{K}\sum_{j=1}^{K} B_{ij}(x, y) P'_i(t) P'_j(t) + O[P'_i(t)^3] \tag{2}$$

where the estimation coefficients A and B are unknown, and K is the number of points at which P' is known, for example, the number of pressure measurement locations. Retaining only the first-order terms in Eq. (2) leads to the LSE:

$$\tilde{\Psi}'(x, y; t) = \sum_{i=1}^{K} A_i(x, y) P'_i(t) \tag{3}$$

For QSE, the first- and second-order terms are retained on the right-hand side in Eq. (2), leading to

$$\tilde{\Psi}'(x, y; t) = \sum_{i=1}^{K} A_i(x, y) P'_i(t) + \sum_{i=1}^{K}\sum_{j=1}^{K} B_{ij}(x, y) P'_i(t) P'_j(t) \tag{4}$$

The objective of SE is to find the coefficients A and B that estimate the velocity using either Eq. (3) or Eq. (4). These coefficients are found through a least-squares procedure that minimizes the mean-square error between the velocity and its estimate [28,45], which involves the sets of two-point correlations between pressure and velocity, which are denoted by:

$$\begin{bmatrix} \overline{P'_1 P'_1} & \cdots & \overline{P'_1 P'_K} \\ \vdots & \ddots & \vdots \\ \overline{P'_K P'_1} & \cdots & \overline{P'_K P'_K} \end{bmatrix} \& \begin{bmatrix} \overline{\Psi' P'_1} \\ \vdots \\ \overline{\Psi' P'_K} \end{bmatrix} \tag{5}$$

For the linear case given in Eq. (3), A is determined from the two-point correlations as follows:

$$A_i(x, y) = \begin{bmatrix} A_1 \\ \vdots \\ A_K \end{bmatrix} = \begin{bmatrix} \overline{P'_1 P'_1} & \cdots & \overline{P'_1 P'_K} \\ \vdots & \ddots & \vdots \\ \overline{P'_K P'_1} & \cdots & \overline{P'_K P'_K} \end{bmatrix}^{-1} \begin{bmatrix} \overline{\Psi' P'_1} \\ \vdots \\ \overline{\Psi' P'_K} \end{bmatrix} \tag{6}$$

Details on the derivation of the estimation coefficients for LSE and QSE can be found in Ukeiley and Murray [14] and Murray and Ukeiley [11], respectively. Based on the number of sensors used in the SE scheme, one can employ SP or MP estimations. The former sets $K = 1$ in Eqs. (3) and (4), whereas the latter involves the summation over K pressure sensors. Both SP and MP methods consist of using single-time realization(s) of the pressure events. In this single-time-delay form of SE, the event vector $P'(t)$ specifies a condition of the wall pressure only at a single time instant. Cole et al. [19] introduced a time delay τ into the estimate to account for a known lag between conditional and unconditional events, yielding the QSE estimate of the velocity as:

$$\tilde{\Psi}'(x, y; t) = \sum_{i=1}^{K} A_i(x, y) P'_i(t - \tau) + \sum_{i=1}^{K}\sum_{j=1}^{K} B_{ij}(x, y) P'_i(t - \tau) P'_j(t - \tau) \tag{7}$$

where τ needs to be determined beforehand.

Durgesh and Naughton [23] extended this framework to one that employs multiple time delays, where information from both past and future events is used in the estimation. Ukeiley et al. [16] took a similar approach, although only using past events. The present study considers the approach proposed by Ukeiley et al. [16], which is referred to as multipoint, multi-time-delay (MP MTD) SE, and yields an estimation of the velocity using past wall-pressure events:

$$\tilde{\Psi}'(x, y; t) = \sum_{d=1}^{N_d} \left[\sum_{i=1}^{K} A_i(x, y) P'_i(t - \tau_d) + \sum_{i=1}^{K}\sum_{j=1}^{K} B_{ij}(x, y) P'_i(t - \tau_d) P'_j(t - \tau_d) \right] \tag{8}$$

where N_d is the number of used pressure events. As will be discussed in Sec. III, the training and validation data sets used for all SE methods are distinct, and so only past samples within the oscillation cycle can be used for the MP MTD method, resulting in a relatively small number of samples used per estimate.

Two main metrics are used to evaluate the quality of the velocity field estimates, the first of which is the average measure of the correlation between the estimated and validation fluctuating velocity fields:

$$\gamma = \frac{\sum_{s=1}^{n} \rho(s)_{\tilde{\Psi}'\Psi'}}{n} \tag{9}$$

where n is the number of points in space, that is, the number of points in the flow field, and $\rho_{\tilde{\Psi}'\Psi'}$ is the cross-correlation coefficient between the estimated ($\tilde{\Psi}'$) and measured (Ψ') fluctuating velocity component fields, which is given by:

$$\rho_{\tilde{\Psi}'\Psi'} = \frac{\mathrm{cov}[\tilde{\Psi}'(t), \Psi'(t)]}{\sigma_{\tilde{\Psi}'(t)}\sigma_{\Psi'(t)}} \tag{10}$$

In addition to the correlation-based metric, the degree to which the estimates resolve the magnitude of velocity fluctuations is assessed. This metric is defined as the ratio of the estimated and measured velocity fluctuation magnitudes, averaged over all spatial locations and time realizations:

$$\kappa = \frac{\sum_{s=1}^{n}\sum_{t=1}^{N} \tilde{\Psi}'(s,t)^2}{\sum_{s=1}^{n}\sum_{t=1}^{N} \Psi'(s,t)^2} \tag{11}$$

where N and n are the number of realizations in time and space, respectively.

III. Experimental Setup

Experiments were conducted in the closed-loop wind tunnel located in the Fluid Mechanics Research Laboratory at the University of Waterloo. The test section is 0.61×0.61 m in cross section and 2.44 m in length and features full optical access. The tunnel has a 9:1 contraction ratio, upstream of which the flow is conditioned by a honeycomb insert and a set of five screens, resulting in a free-stream turbulence intensity of less than 0.1%. Furthermore, the incoming flow was verified to have no significant spectral content within the frequency range of interest to this investigation, $150 < f < 1500$ Hz. The flow uniformity in the test section is within $\pm 0.5\%$ over 95% of the test section span. The free-stream velocity was set based on the static pressure drop across the contraction calibrated against a Pitot-static tube in the empty test section, with the associated uncertainty in the free-stream velocity estimated to be less than 2%.

Tests were performed using a NACA 0018 airfoil model with a chord length of $c = 0.2$ m and a span of 0.61 m. The airfoil model was set to an aerodynamic angle of attack of $\alpha = 4°$, and measurements were performed at a chord-based Reynolds number of 125,000. A surface-attached coordinate system is used for data presentation, where x, y, and z correspond to the wall-tangent, wall-normal, and spanwise directions (Fig. 1), respectively, with the origin at the leading edge of the mid-span plane. The airfoil model is equipped with 25 Panasonic WM-62C back electret condenser microphones installed under 0.8-mm-diam ports, which are distributed along the chord in a row located at $z/l = 0.2$ (Fig. 1c), where l is the surface arc length from the leading to the trailing edge. Each microphone was calibrated in the airfoil model relative to a reference 4189 Brüel and Kjær microphone. All microphones have a constant response (± 1 dB) in the range $150 < f < 1500$ Hz. Further details on the airfoil model design, fabrication, and instrumentation are available in Gerakopulos and Yarusevych [46]. For the purposes of the present study, seven of the microphones located within the field of view of the velocity measurements, at $x/l = 0.36, 0.40, 0.44, 0.48, 0.52, 0.57$, and 0.60 (Fig. 1), are considered for SE. All microphones were sampled simultaneously at 40 kHz and low-pass filtered at 20 kHz using a National Instruments PCI-4472 data acquisition card.

Time-resolved, two-component particle image velocimetry (PIV) was used to acquire velocity fields in a chordwise oriented plane at $z/l = 0$ (Fig. 1). The flow was seeded using a glycol-water based fog with a mean particle diameter on the order of one micrometer and illuminated by a laser sheet produced by a Photonics DM20-527 Nd:YLF pulsed laser. The laser beam was introduced through the side wall of the test section and conditioned into a sheet approximately 1 mm thick. Images were captured by two Photron SA4 high-speed cameras arranged in downstream succession and synchronized with the laser via a LaVision high-speed timing unit controlled through LaVision's DaVis 8 software. Equal magnification factors of 0.67 were set for the cameras and the fields of view were overlapped by 10%, which after stitching yielded a combined field of view of 55 mm × 14.5 mm. The particle images were acquired at a sampling frequency of 3.8 kHz, which is approximately five times greater than the dominant flow frequency of interest. Images were processed in LaVision's DaVis 8 software using a multipass, iterative cross-correlation algorithm with decreasing window size. The final window size was 16×16 pixels, with 75% overlap, yielding a vector pitch of 0.12 mm. The results were postprocessed using universal outlier detection [47]. Once the vector fields were calculated, the mean velocity fields for each camera were cross-correlated in the overlap region to align the fields of view, and the fields were then stitched using a cosine weighted blending function in the overlap region. The random errors in the PIV measurements were evaluated using the correlation statistics method [48], with the associated uncertainty in the average velocity field estimated to be less than 6% of the free-stream velocity within the region of the separated shear layer.

PIV and microphone measurements were acquired simultaneously to enable SE. Note that the spanwise locations of the microphones and the laser sheet were offset by $0.2l$ to mitigate surface reflections from microphone ports in the PIV measurements (Fig. 1b). Kurelek et al. [49,50] demonstrated that the dominant shear layer structures for these flow conditions have a relatively high spanwise coherence in the fore part of the field of view, making it possible to employ SE schemes to estimate the coherent component of velocity fluctuations

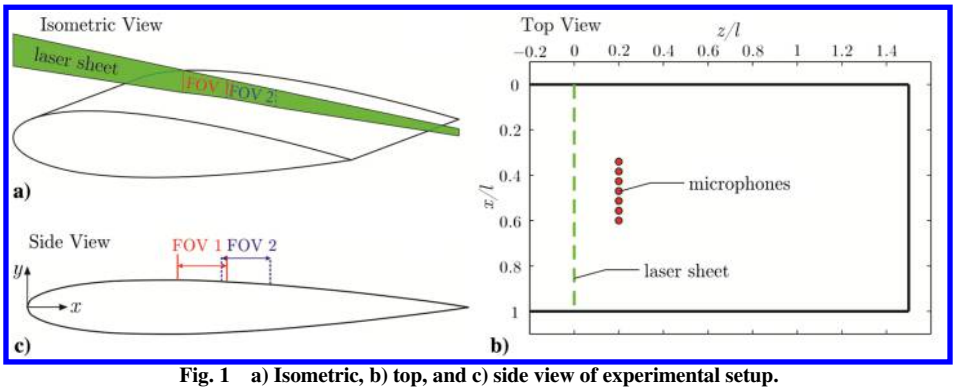

Fig. 1 a) Isometric, b) top, and c) side view of experimental setup.

based on wall pressure fluctuations in the proximity of the PIV measurement plane.

The synchronized PIV and microphone measurements were divided into two sets: 1) a training set containing 4000 velocity fields and matching surface pressure measurements, and 2) a validation set containing 1000 velocity fields. The SE coefficients [Eqs. (3) and (4)] were determined using the training data set, and the performance of each SE method was evaluated through comparison with the validation set. Therefore, the number of realizations in Eqs. (9) and (11) is 1000. SP estimation uses pressure events measured by a single microphone, whereas MP estimation uses all seven microphones, with both methods using information at a single time instant to estimate the corresponding velocity field. On the other hand, the MP MTD method uses past and present pressure events for all microphones within the field of view.

IV. Results

In this section the SE techniques discussed in Sec. II are used to estimate velocity fields for a separation bubble formed over a NACA 0018 airfoil at $Re = 125{,}000$ and $\alpha = 4°$. First, through analysis of the velocity and surface pressure fluctuations, the main characteristics of the separation bubble are established, and the applicability of SE is demonstrated. This is followed by the evaluation of the SP, MP, and MP MTD SE techniques, for which the linear and quadratic formulations are considered and contrasted.

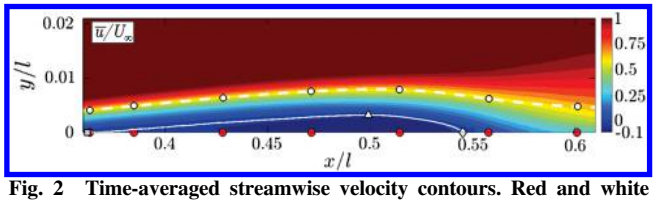

Fig. 2 Time-averaged streamwise velocity contours. Red and white circles indicate pressure sensor locations and the corresponding streamwise locations along the displacement thickness (white dashed line), respectively.

A. Separation Bubble Characteristics

The mean streamwise topology of the separation bubble is illustrated in Fig. 2 using time-averaged contours of the streamwise velocity component. The mean bubble outline is defined by the contour of zero streamwise velocity [51] and is identified in Fig. 2 by the white solid line. This contour bounds the region of reverse flow near the surface and is used to estimate the mean streamwise locations of separation, $x_S/l = 0.36$, maximum bubble height, $x_H/l = 0.50$, and reattachment, $x_R/l = 0.55$, which are denoted by the white square, triangle, and diamond symbols, respectively. The displacement thickness, δ^* (dashed line in Fig. 2) tracks the core of the shear layer where, as will be shown later, velocity fluctuations experience significant amplification.

The streamwise growth of disturbances in the bubble is analyzed via spectra of the wall-normal velocity fluctuations sampled along the displacement thickness and at the streamwise locations of the pressure sensors (white dots in Fig. 2). The results are shown in Fig. 3a alongside spectra of the surface pressure fluctuations (Fig. 3b). Note that the velocity and pressure spectra have frequency resolutions of 2 and 0.76 Hz, respectively. The results of Fig. 3a show amplification of disturbances in the separated shear layer within a band of frequencies centered at $f = 750$ Hz, which is indicated by the gray dashed lines. The broad spectral peaks centered at this frequency in both the velocity and surface pressure spectra within $0.44 < x/l < 0.57$ suggest that the velocity and surface pressure fluctuations are likely well correlated in this region [52]. Farther downstream ($x/l \geq 0.57$), energy is redistributed to a much broader range of frequencies, indicating the transition to turbulence. It should be noted that relatively broadband yet elevated energy levels are detected in the spectra at $f \approx 280$ Hz (gray dotted lines in Fig. 3), most notably in the pressure spectra. This is linked to the presence of an acoustic standing wave in the test section, which is typical for any hard-walled wind tunnel section. However, the associated frequency is sufficiently removed from the shear layer's unstable frequency band, and therefore the noted acitivty is not expected to influence the flow development or shear layer transition process.

As the primary focus of this work concerns the SE of velocity fields through surface pressure measurements, it is important to establish

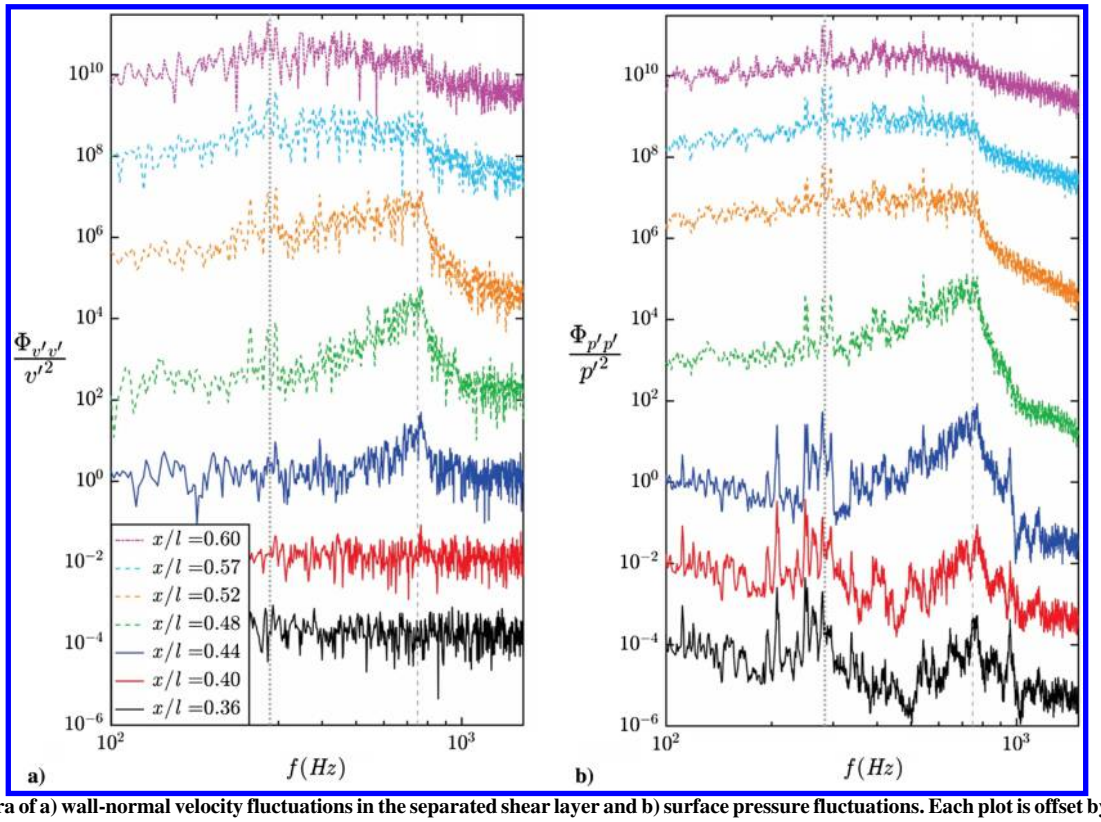

Fig. 3 Spectra of a) wall-normal velocity fluctuations in the separated shear layer and b) surface pressure fluctuations. Each plot is offset by one order of magnitude for clarity.

the correlation between the velocity field and the measured surface pressures. To this end, a sequence of instantaneous spanwise vorticity contours within the laminar separation bubble is shown in Figs. 4a–4f. Presented alongside in Figs. 4g and 4h are time signals of the streamwise and wall-normal velocity fluctuations measured at $x/l = 0.52$ in the separated shear layer (white dot in Figs. 4a–4f), followed by surface pressure fluctuations at the same streamwise location (red dot in Figs. 4a–4f) in Fig. 4i. Each snapshot in the vorticity sequence is assigned a marker, which are used throughout Figs. 4g–4i. In Figs. 4a–4f, the field of view begins downstream of separation and shows the roll-up of the shear layer and shedding of vortices. Coherent vortical structures are first identifiable upstream of the maximum mean bubble height location ($x_H/l = 0.50$), with mean reattachment following shortly downstream ($x_R/l = 0.55$). Downstream of the reattachment point, these structures break down to smaller scales, which is marked in the velocity spectra (Fig. 3a) by the redistribution of energy to a broad range of frequencies. In identifying and tracing two vortices, labeled as V_1 and V_2, the correlation between the passage of these structures and the velocity and pressure signals is established. For example, at t_4, the center of vortex V_2 is directly above the pressure sensor p_5, which is associated with a local minimum in the fluctuating pressure (Fig. 4i), while the fluctuating streamwise and wall-normal velocity (Figs. 4g and 4h, respectively) are phase shifted by $\pi/2$ and π, respectively, with respect to the surface pressure. Thus, the dominant flow structures produce a distinct signature in the surface pressure fluctuations; however, as expected, there are substantial phase shifts between velocity and surface pressure fluctuations that need to be accounted for in the SE schemes.

Figure 5 depicts the spatial distribution of cross-correlation coefficients between surface pressure and velocity fluctuations from the training data set. The correlation between surface pressure fluctuations and both streamwise and wall-normal velocity fluctuations is examined for two surface pressure sensors, p_4 ($x/l = 0.48$) and p_5 ($x/l = 0.52$). These sensors are selected because they are closest to the maximum bubble height location (Fig. 2), and as a result measure the largest amplitude velocity and pressure fluctuations (Fig. 3), which is directly linked to the roll-up and formation of the shear layer vortices (Fig. 4). The results in Fig. 5 confirm the strong correlation between velocity fields and surface pressure fluctuations. As expected, the highest correlation coefficients are seen at the streamwise location matching that of the sensor, and cross-correlation coefficient magnitudes decrease as the streamwise distance from the sensor increases. It is evident that the maximum cross-correlation coefficient depends on the position of the selected pressure sensor, with stronger correlation observed for sensor p_4 compared with p_5. This implies that the effectiveness of a given SE scheme will depend on the pressure sensor(s) used in the estimation. Furthermore, the most reliable predictions are expected in the region where strong shear layer vortices are observed. In contrast, low predictive capabilities can be expected in the fore portion of the bubble and downstream of mean reattachment, where the magnitude of coherent perturbations are relatively weak.

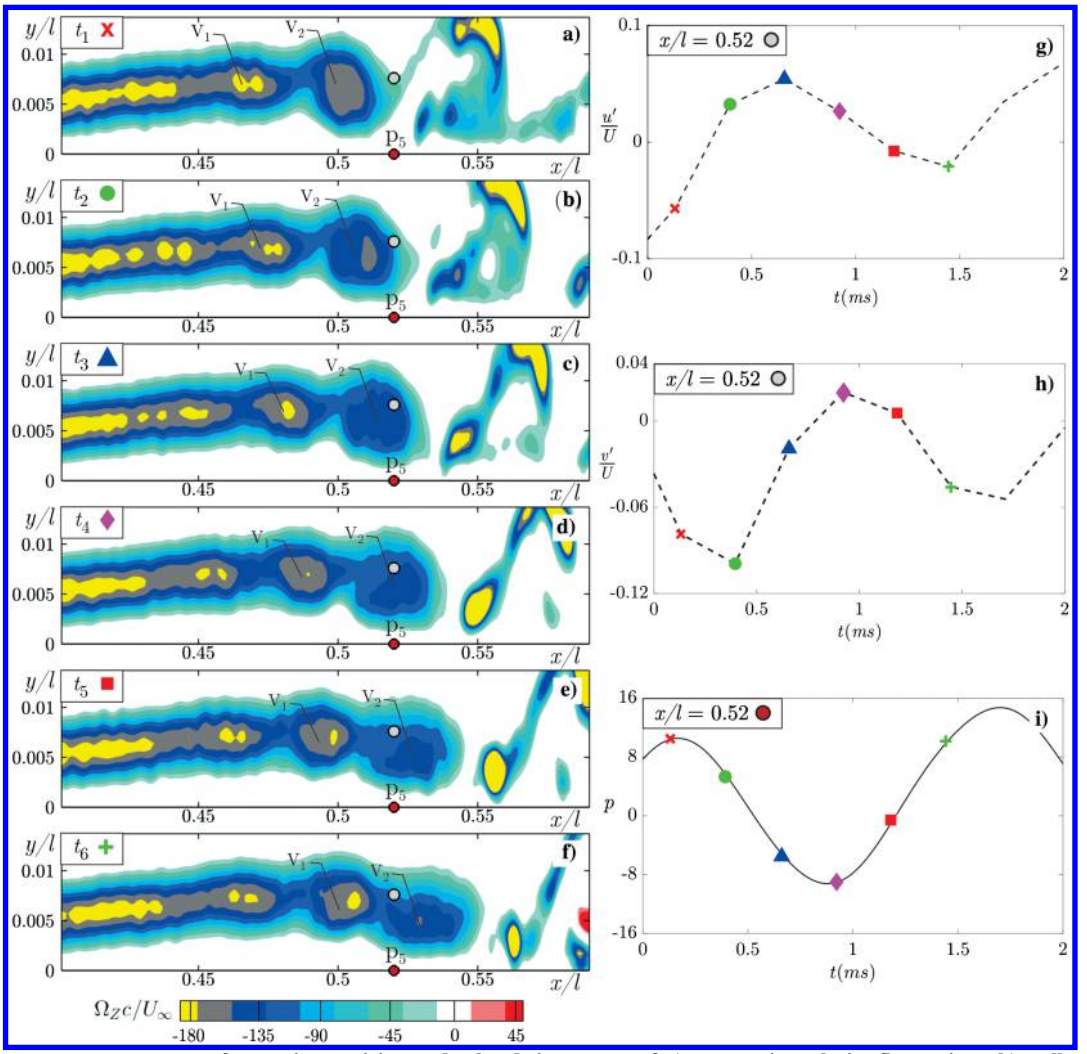

Fig. 4 a–f) Instantaneous contours of spanwise vorticity, and related time traces of g) streamwise velocity fluctuations, h) wall-normal velocity fluctuations, and i) surface pressure fluctuations.

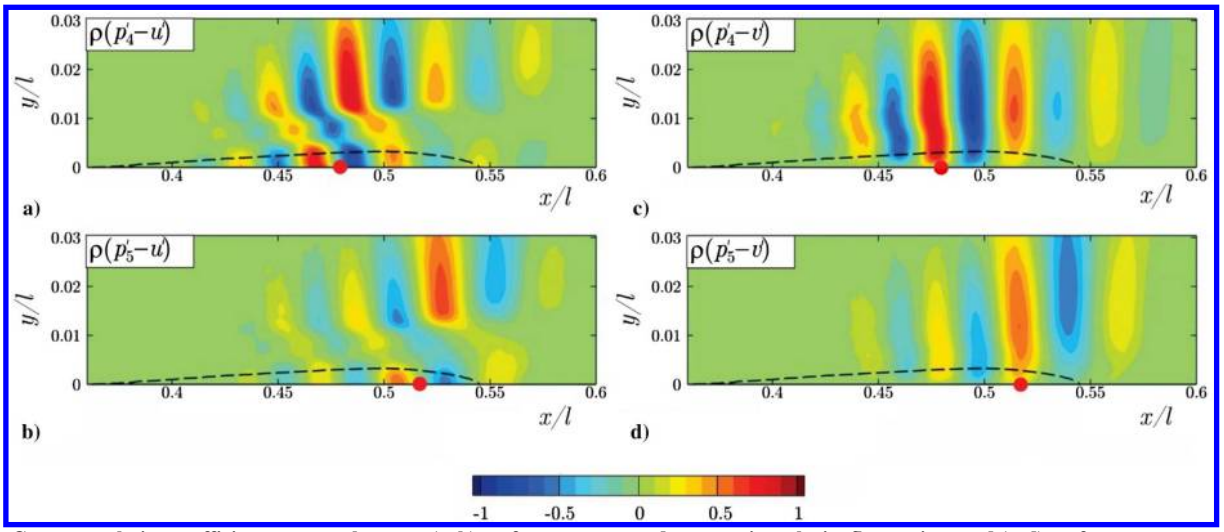

Fig. 5 Cross-correlation coefficient contours between (a, b) surface pressure and streamwise velocity fluctuations and (c, d) surface pressure and wall-normal velocity fluctuations. Red markers indicate the pressure sensor employed. Dashed lines indicate the outline of the reverse flow region.

B. Stochastic Estimation

First, it is instructive to consider the SP STD LSE approach. To determine the optimum sensor for the SP method, velocity field estimates are made using sensors p_1 to p_7. The quality of the estimates is characterized using the average cross-correlation coefficient and fluctuating velocity magnitude ratio metrics [Eqs. (9) and (11), respectively], with the results presented in Fig. 6. The results show that the average correlation between the estimated and validation velocity fields (Figs. 6a and 6c) increases as pressure sensors located closer to the maximum height of the bubble (located approximately at p_5) are used. In the fore portion of the bubble, sensors p_1 and p_2 yield average correlation coefficients of approximately 5%. Moving downstream to sensors p_3 to p_6, the correlation coefficients increase, reaching maxima of approximately 13% and 15% at sensor p_4 for the streamwise and wall-normal velocity fluctuations, respectively. The fluctuating velocity magnitude ratios (Figs. 6b and 6d) follow a similar trend, as values are relatively low in the fore portion of the bubble, while maximum values of approximately 13% (u') and 16% (v') are found at sensors p_6 and p_5, respectively. Based on an aggregate of all performance metrics presented in Fig. 6, sensor p_5 is selected as optimal, and therefore is used when comparing the SP method to the other SE methods considered.

Durgesh and Naughton [23] demonstrated that an optimum time delay exists for the MP MTD method when distinct training and validation data sets are employed, as is the case for this investigation. To determine this optimum value, a wide range of time delays, $\tau = 0$ to $0.75t^*$ (corresponding to $N_d = 0$ to 50), are employed and performance is compared using the cross-correlation coefficient metric, with the results plotted in Fig. 7. It is important to note that $\tau = 0$ ($N_d = 0$) corresponds to the MP method (i.e., no past events used), and so a significant increase in performance is realized when the time delay is increased to a nonzero value. More moderate increases in performance are found as the time delay is increased

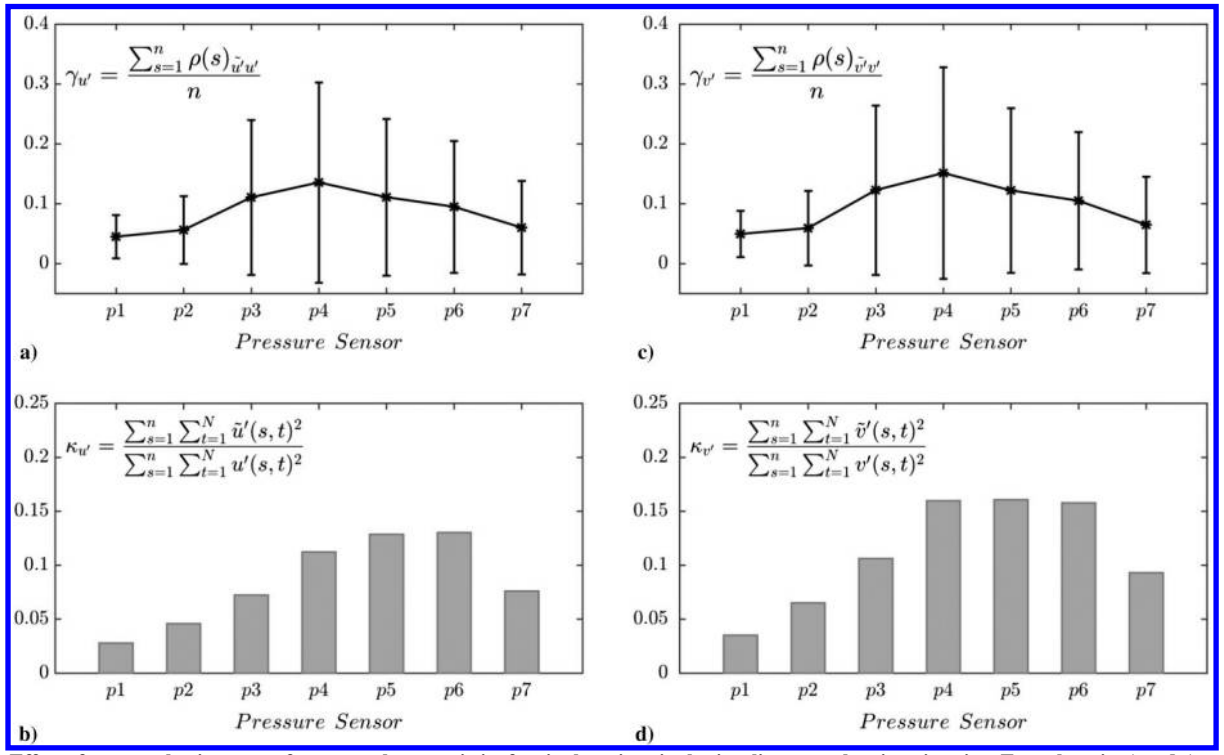

Fig. 6 Effect of sensor selection on performance characteristics for single-point, single-time linear stochastic estimation. Error bars in a) and c) are based on twice the standard deviation of the cross-correlation coefficient.

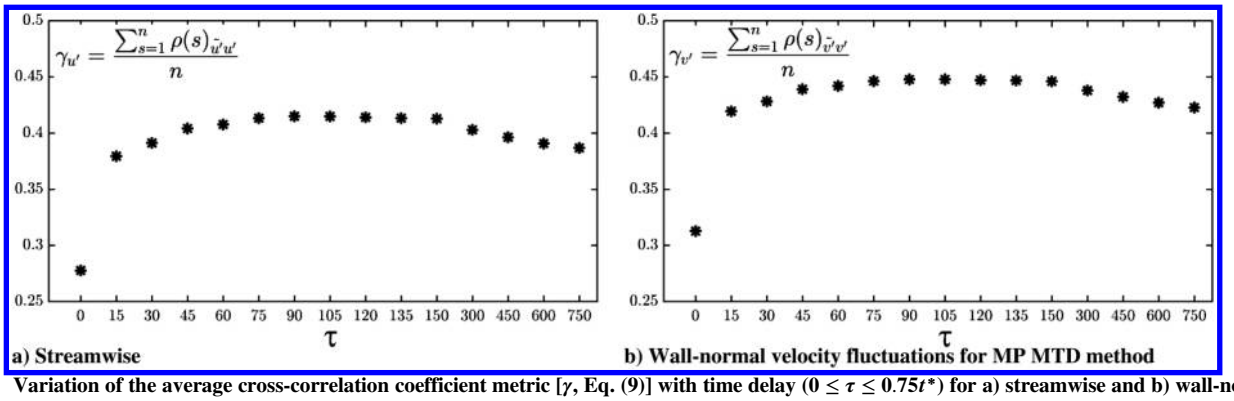

Fig. 7 Variation of the average cross-correlation coefficient metric [γ, Eq. (9)] with time delay ($0 \leq \tau \leq 0.75t^*$) for a) streamwise and b) wall-normal velocity fluctuations for MP MTD method.

further, reaching a peak value at $\tau = 0.105t^*$ corresponding to $N_d = 7$, which is selected as the time delay for the MP MTD methods.

Having determined the optimum sensor and time delay for the SP and MP MTD methods, respectively, the performance across all SE formulations is compared in Fig. 8. Across all metrics, accuracy increases significantly when information from multiple sensors is included in the estimate (SP vs MP methods), and then further by the inclusion of past time events (MP vs MP MTD). For example, Fig. 8d shows that the ratio of resolved wall-normal velocity fluctuation magnitude increases from 16 to 35% when moving from SP LSE to MP LSE, and then further increases to 54% when MP MTD LSE is employed. A similar trend is seen in γ (Figs. 8a and 8c), although the improvements are more moderate. In contrast, the inclusion of quadratic terms has a less significant impact. For the SP and MP methods, the use of QSE leads to negligible improvements relative to LSE (e.g., γ increases from 28 to 29% in comparing MP LSE and QSE in Fig. 8a). A noteworthy increase due to QSE is seen only for the MP MTD method, where the fluctuation velocity magnitude ratio increases by approximately 8% (Figs. 8b and 8d). Thus, in the present investigation, the additional processing time associated with QSE is only worthwhile for the MP MTD method. A similar observation is noted by Caraballo et al. [30] for cavity flows.

The ability of the SE techniques to reconstruct the spatial organization of the flow field is assessed in Fig. 9, where contours of streamwise and wall-normal RMS velocity fluctuations are presented. Results for the measured flow field are presented in Figs. 9d and 9h, and show a strong concentration of high-amplitude fluctuations just above the outline of the reverse flow region, that is, within the separated shear layer, with strong streamwise growth in both u'_{rms} and v'_{rms} occurring up- and downstream of where the reverse flow region attains its maximum height. This topology is consistent with that reported in previous studies [42,53,54] and serves as the basis for comparison with results from the SP, MP, and MP MTD QSE methods. Both the SP and MP methods fail at providing a global description of the RMS fields, instead producing estimates that appear phase-locked to the predictor, which is attributed to neglecting the time lag that exists between the pressure and velocity events. These methods are unable to reproduce the fluctuations at all phases of the flow. On the other hand, the MP MTD QSE method (Figs. 9c and 9g) outperforms the others in terms of estimating both the spatial

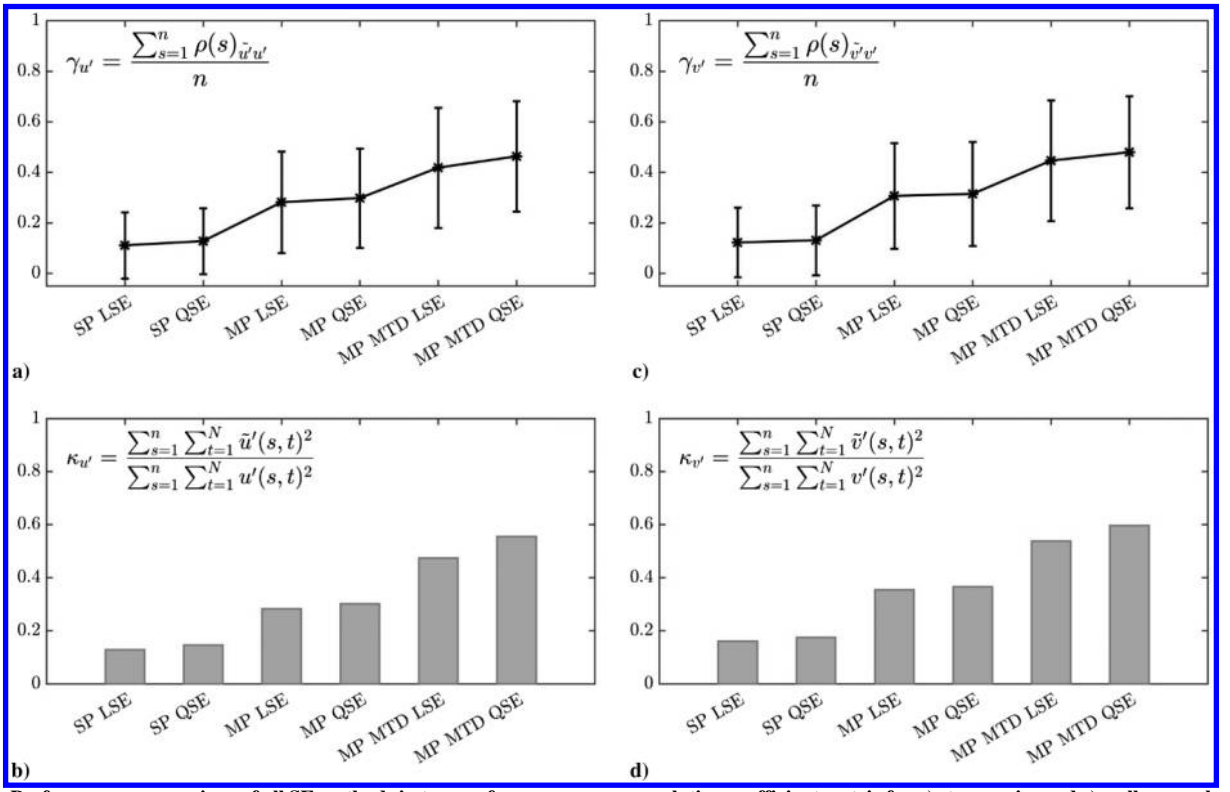

Fig. 8 Performance comparison of all SE methods in terms of average cross-correlation coefficient metric for a) streamwise and c) wall-normal velocity fluctuations, and fluctuating velocity magnitude ratio metric for b) streamwise and d) wall-normal velocity fluctuations.

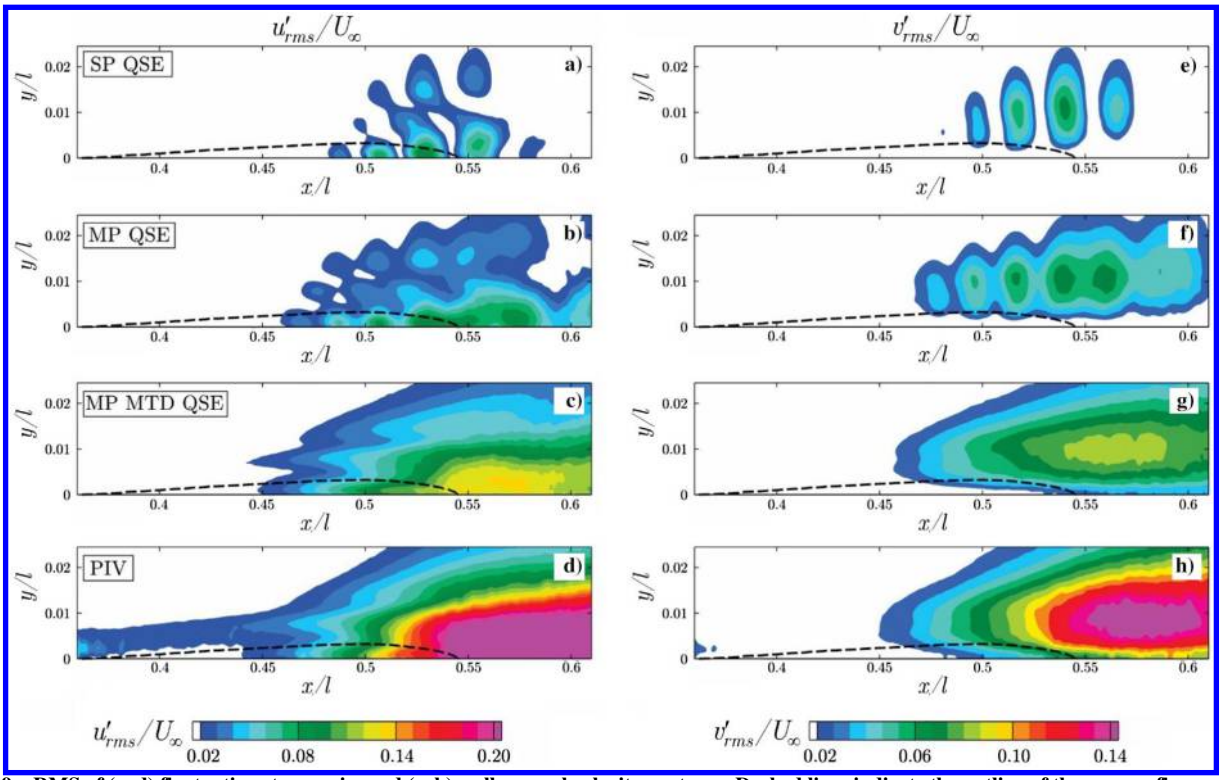

Fig. 9 RMS of (a–d) fluctuating streamwise and (e–h) wall-normal velocity contours. Dashed lines indicate the outline of the reverse flow region.

distribution and local magnitudes of u'_{rms} and v'_{rms} due to its ability to overcome time lag between the pressure and velocity events.

In addition to estimating statistical quantities, it is also of interest to evaluate the ability of the SE methods to estimate the time-resolved dynamics within the separation bubble. Figure 10 shows exemplary segments of measured temporal velocity fluctuation signals sampled at two streamwise locations along the displacement thickness, which are compared with signals reconstructed using SP, MP, and MP MTD QSE. Excellent agreement is found between the measured and MP MTD signals, as the signals are generally in-phase and agree in amplitude, with under predictions only occurring at a few instants, for example, at $t = 8$ ms in Figs. 10c and 10d. In contrast, a notably lower agreement with the validation set is seen for the MP QSE method, and even more so for the SP method, as both show phase mismatch over certain time intervals and do not estimate the amplitude of fluctuations as closely as the MP MTD results. It is worth noting that the results of SP QSE are improved at $x/l = 0.52$ (Figs. 10c and 10d) compared with $x/l = 0.48$ (Figs. 10a and 10b), indicating that the performance of the SP method deteriorates significantly with increasing distance from the location of the sensor, which is located at $x/l = 0.52$.

To assess the frequency content of the stochastic estimates, spectra of the measured and reconstructed fluctuating velocity signals presented in Fig. 10 are shown in Fig. 11. As expected, the spectra of the MP MTD estimates closely match the validation results, with excellent agreement seen across the entire frequency domain of interest and in particular at frequencies near 750 Hz (dashed line in Fig. 11), with this activity linked to the vortex shedding phenomenon. The MP method is also able to accurately resolve the frequency of velocity fluctuations; however, the spectral energy levels are underpredicted. Once again, the accuracy of predicted spectra decreases significantly for the SP method, which fails to accurately capture the frequency and associated energy of dominant fluctuations, except for the wall-normal velocity fluctuations at $x/l = 0.52$.

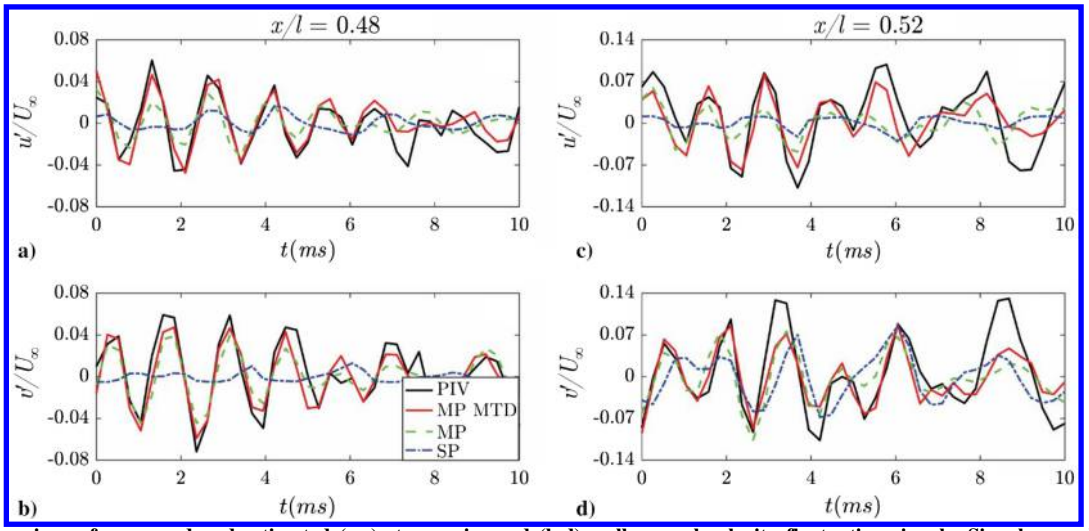

Fig. 10 Comparison of measured and estimated (a,c) streamwise and (b,d) wall-normal velocity fluctuation signals. Signals sampled at $y = \delta^*$, $x/l = 0.48$ and 0.52.

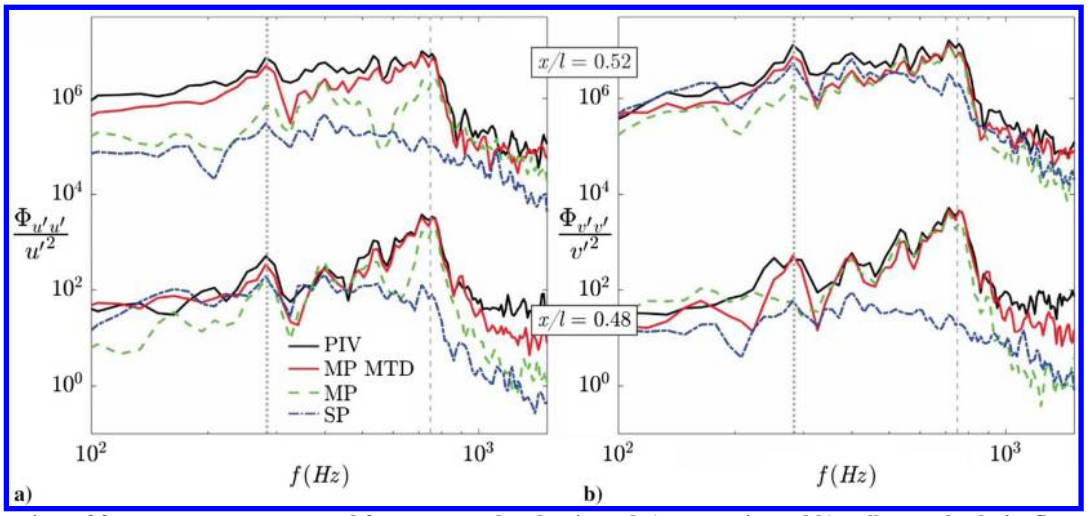

Fig. 11 Comparison of frequency spectra computed from measured and estimated a) streamwise and b) wall-normal velocity fluctuations. Signals sampled at $y = \delta^*$, $x/l = 0.48$ and 0.52.

So far, the assessment of the fluctuating velocity signals reconstructed using SE has been confined to locations within the bubble where velocity disturbance amplitudes are relatively large, and the pressure and velocity signals are well-correlated. To highlight the effect of location within the bubble, fluctuating velocity magnitude ratios are calculated between estimated and validation signals at different streamwise positions within the bubble, with the results presented in Fig. 12a. Note that the results pertain to temporal signals sampled at $y = \delta^*$. To aid in the discussion, Figs. 12b and 12c are presented alongside, which show contours of the cross-correlation coefficients between the fluctuating velocity fields and surface pressure, averaged across all pressure sensors. Beginning with the cross-correlation coefficients, the velocity fluctuations are well correlated with the pressure fluctuations within the vicinity of the maximum mean bubble height location ($x_H/l = 0.50$) and, as a result, the magnitude of velocity fluctuations is relatively well resolved (i.e., highest values of κ are found) in this region (Fig. 12a). Comparatively, the cross-correlation coefficients decrease with increasing distance from the maximum bubble height location in both the up- and downstream directions, and so the value of κ decreases away from $x_H/l = 0.50$. In the upstream direction, as the separation point is approached, the correlation degrades as a result of small amplitude of velocity and pressure fluctuations in this region. On the other hand, for the region downstream of turbulent reattachment, the fluctuations in this region are distributed across a wide band of frequencies (cf., Fig. 3), yielding diminishing correlations between velocity and pressure.

In considering each method examined in Fig. 12a, the SP method shows relatively low values of κ at all streamwise locations, save for at $x/l = 0.52$ (i.e., the location of the employed pressure sensor), which again highlights the weakness of the SP method in resolving the global flow field. Increases in κ are seen at all streamwise positions when moving from the SP to the MP method, particularly at $x/l = 0.48$, where κ reaches approximately 0.4 and 0.6 for u' and v', respectively. This relatively large gain in accuracy is attributed to the estimate using information from nearby sensors in a region where velocity fluctuations in the shear layer are well correlated with surface pressure fluctuations (Figs. 12b and 12c). Further increases in κ are seen when the MP MTD method is employed, as values of 0.8 for both u' and v' are attained at $x/l = 0.48$. However, it is important to note that such dramatic gains are not realized near mean separation, nor downstream of mean reattachment. In the fore portion of the bubble, this can be attributed to the relatively low amplitude of the disturbances (Figs. 9d and 9h), leading to random noise dominating both the PIV and pressure measurements. Downstream of reattachment, a different effect is at play, as coherent structures

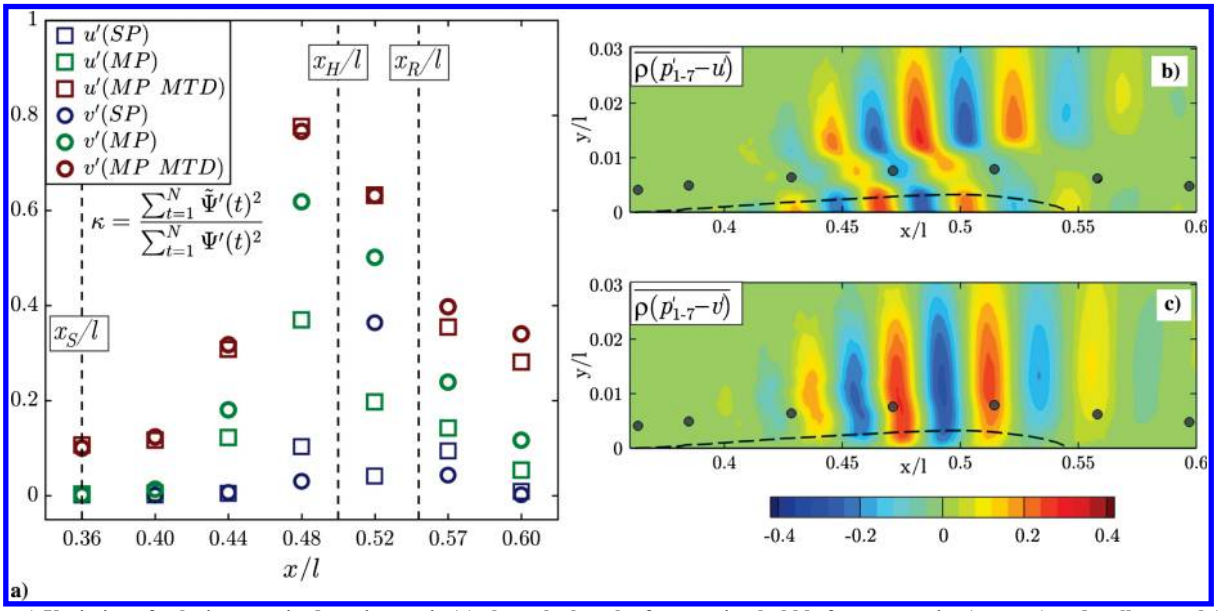

Fig. 12 a) Variation of velocity magnitude ratio metric (κ) along the length of separation bubble for streamwise (squares) and wall-normal (circles) velocity fluctuations. Contours of mean cross-correlation coefficients between surface pressure and b) streamwise and c) wall-normal velocity fluctuations.

breakup (Fig. 4) during the later stages of transition, and both velocity and pressure fluctuations become increasingly random. Consequently, surface pressure and velocity fluctuations become progressively less correlated, as seen in Figs. 12b and 12c, and all SE methods perform relatively poorly in this region. It should be noted that in the vortex breakup region moderate performance gains can be attained through more advanced SE techniques (i.e., MP and MP MTD over SP), whereas this is not the case near the separation point where minute fluctuations in the flow field cannot be accurately measured.

The ability of the SE methods to capture the development of the dominant coherent structures in the separation bubble is examined in Fig. 13, where a sequence of instantaneous vorticity contours is presented. Contours of the λ_2 criterion [55] are added to aid in the detection of vortical structures, and dashed lines are added to assist in tracking individual vortices between frames. From the measured sequence (Figs. 13a–13d), the flow development is characterized by the roll-up of the separated shear layer into periodic vortical structures, which are shed, convect downstream, and eventually breakdown to smaller scales. The observed shear layer dynamics are not captured in the SP results (Figs. 13e–13h). The presence of shear layer vortices is only adequately resolved at $t = 6$ ms (Fig. 13g), which is likely due to the vortex passing over the employed sensor (at $x/l = 0.52$), leading to a strong correlation between the surface pressure and velocity field at this time instant. This shortcoming is alleviated by the MP method (Figs. 13i–13l), as the entire train of vortices is identifiable throughout the sequence and their streamwise progression can be tracked. However, in comparison to the measured sequence, the smaller-scale structures associated with the vortex deformations in the aft portion of the bubble are not captured by the MP estimates. These features are captured in the MP MTD results (Figs. 13m–13p), which is consistent with MP MTD's superiority in resolving temporal, spectral, and statistical characteristics of the separation bubble's velocity field (Figs. 9–12).

It is clear that, although both the MP QSE and MP MTD QSE methods are able to describe the general development of the shear layer vortices (Fig. 13), there may be differences in estimated vortex

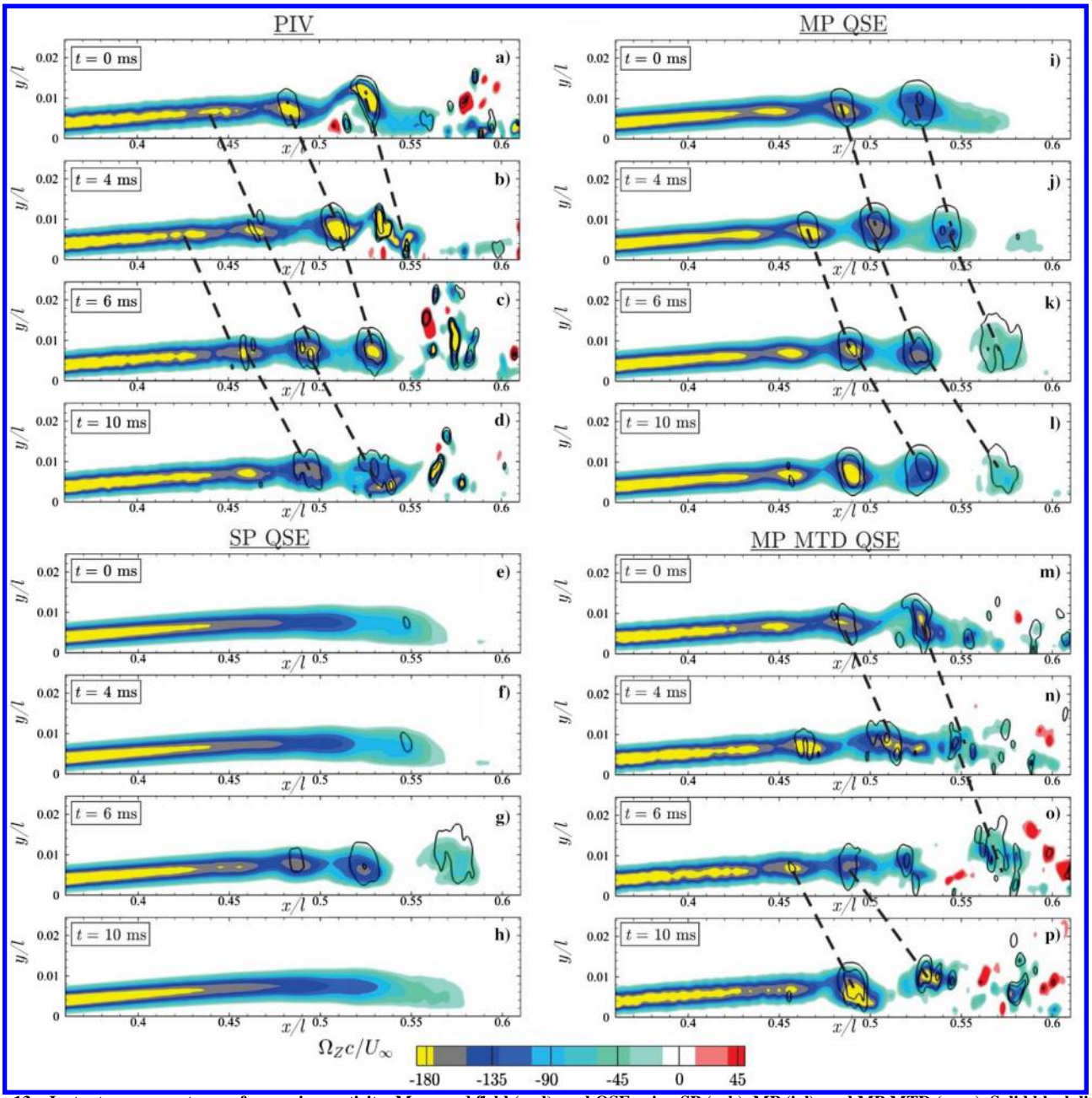

Fig. 13 Instantaneous contours of spanwise vorticity. Measured field (a–d), and QSE using SP (e–h), MP (i–l), and MP MTD (m–p). Solid black lines indicate λ_2-contours [55]. Dashed black lines trace the same vortices through the sequence.

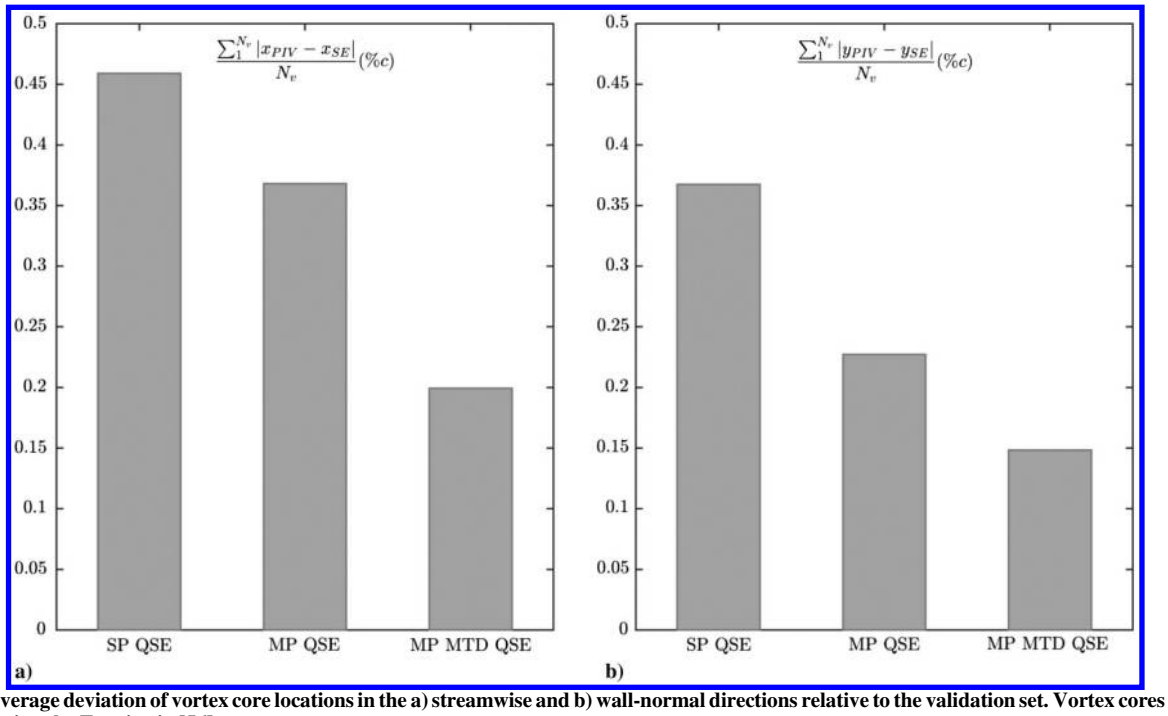

Fig. 14 Average deviation of vortex core locations in the a) streamwise and b) wall-normal directions relative to the validation set. Vortex cores locations identified using the Γ_1 criteria [56].

locations. This is quantified using the Γ_1 criterion [56] for the identification of vortex cores. This method avoids the sensitivity errors in vortex core detection due to small-scale turbulence by employing a global quantity, that is, solid body rotation, and identifies vortex cores based on local peaks of Γ_1, which typically range from 0.9 to 1 near a vortex core. Using this method, vortex core locations are identified in the estimated flow fields from SP, MP, and MP MTD and their location is then compared with that determined from the validation set. Specifically, for each vortex core detected in the validation set, the closest vortex core is identified in the corresponding estimated field, and the deviations in both the streamwise and wall-normal directions are quantified. For each SE method, the average deviations in vortex core location are then determined, with the results presented in Fig. 14. Note that this approach does not account for missed detections in the reconstructions, because in such instances no deviation is recorded. As expected, the results in Fig. 14 show that the accuracy in determining vortex core locations increases as the SE method is improved from SP to MP, and then again from MP to MP MTD. The average deviations for the MP MTD method are 0.2 and 0.15% of the chord in the x and y directions, respectively, which indicates that, on average, vortex core locations are accurately captured in SE results, because these values are an order of magnitude smaller than the size and streamwise wavelength of the vortices, both of which are on the order of 5% of c.

V. Conclusions

The present investigation examined the effectiveness of several surface-pressure-based stochastic estimation (SE) methods in reconstructing the velocity field of a separation bubble formed over a NACA 0018 airfoil at a chord Reynolds number of 125,000 and an angle of attack of 4°. For all the SE methods examined, the accuracy of the estimates is the highest in the region centered on the mean maximum bubble height location ($0.44 < x/l < 0.57$), where strongly coherent velocity and pressure fluctuations are present and measurable. These fluctuations are the result of the amplification of background disturbances in the separated shear layer, leading to shear layer roll-up and the formation of coherent and strongly periodic vortical structures. Outside of this region, the accuracy of the estimates is decreased markedly, specifically toward the mean separation point where the low-amplitude disturbances cannot be accurately measured, and downstream of mean reattachment where the transition to turbulence increases the randomness of the fluctuations. However, it is demonstrated that moderate performance gains can be attained downstream of mean reattachment through more advanced SE techniques.

Several SE methods were investigated in order to elucidate the effects of the number of events (in time and space) and the inclusion of higher-order terms on the accuracy of the estimates. Instantaneous velocity fields were reconstructed using SE methods, which were compared with the measured (validation) fields in terms of time-averaged statistics, temporal and spectral content, and spatial organization. The accuracy of the estimates was quantified through the evaluation of two metrics, namely the average cross-correlation coefficient between estimated and validation quantities, and the ratio of fluctuating velocity magnitudes between estimated and validation fields. A comparison of the single-point (SP) and multipoint (MP) methods has shown that the accuracy of the estimates, with respect to both metrics employed, is increased substantially through the inclusion of additional simultaneous predictor events in space. Similarly, through the additional inclusion of past predictor events, that is, the MP multi-time-delay (MTD) method, further increases in accuracy are realized, resulting in the capture of flow features across all scales of interest and a reconstructed flow field that most closely matches the validation data. Furthermore, through the comparison of the linear and quadratic stochastic estimation techniques, it is shown that the inclusion of higher-order terms provides negligible benefit for the SP and MP methods, whereas a moderate improvement is achieved for the MP MTD method. Thus, in allocating resources for SE, priority should be given to increasing the number of predictor events, after which higher-order methods may be considered.

The results of this investigation conclusively show that SE is a viable tool for real-time diagnostics of a separation bubble flow. In particular if the MP technique or MP MTD technique is considered, SE can be successfully implemented to predict salient dynamic characteristics of a separation bubble.

Acknowledgments

The authors would like to acknowledge the financial support of the Natural Sciences and Engineering Research Council of Canada (NSERC) and the Ontario Centers of Excellence (OCE) TalentEdge Fellowship Program (TFP) under Project Number 25657.

References

[1] Adrian, R. J., "On the Role of Conditional Averages in Turbulence Theory," *Turbulence in Liquids; Proceedings of the Fourth Biennial Symposium*, Science Press, Princeton, NJ, 1977, pp. 323–332.

[2] Adrian, R. J., "Conditional Eddies in Isotropic Turbulence," *The Physics of Fluids*, Vol. 22, No. 11, 1979, pp. 2065–2070. doi:10.1063/1.862515

[3] Choi, W. C., and Guezennec, Y. G., "On the Asymmetry of Structures in Turbulent Boundary Layers," *Physics of Fluids A: Fluid Dynamics*, Vol. 2, No. 4, 1990, pp. 628–630. doi:10.1063/1.857711

[4] Naguib, A. M., Wark, C. E., and Juckenhöfel, O., "Stochastic Estimation and Flow Sources Associated with Surface Pressure Events in a Turbulent Boundary Layer," *Physics of Fluids (1994–Present)*, Vol. 13, No. 9, 2001, pp. 2611–2626. doi:10.1063/1.1389284

[5] Adrian, R. J., and Moin, P., "Stochastic Estimation of Organized Turbulent Structure: Homogeneous Shear Flow," *Journal of Fluid Mechanics*, Vol. 190, May 1988, pp. 531–559. doi:10.1017/S0022112088001442

[6] Ewing, D., and Citriniti, J. H., "Examination of a LSE/POD Complementary Technique Using Single and Multi-Time Information in the Axisymmetric Shear Layer," *IUTAM Symposium on Simulation and Identification of Organized Structures in Flows*, Springer, The Netherlands, 1999, pp. 375–384.

[7] Picard, C., and Delville, J., "Pressure Velocity Coupling in a Subsonic Round Jet," *International Journal of Heat and Fluid Flow*, Vol. 21, No. 3, 2000, pp. 359–364. doi:10.1016/S0142-727X(00)00021-7

[8] Taylor, J. A., and Glauser, M. N., "Towards Practical Flow Sensing and Control via POD and LSE Based Low-Dimensional Tools," *Journal of Fluids Engineering*, Vol. 126, No. 3, 2004, pp. 337–345. doi:10.1115/1.1760540

[9] Hudy, L. M., Naguib, A., and Humphreys, W. M., "Stochastic Estimation of a Separated-Flow Field Using Wall-Pressure-Array Measurements," *Physics of Fluids*, Vol. 19, No. 2, 2007, Paper 024103.

[10] Sicot, C., Perrin, R., Tran, T. T., and Boree, J., "Wall Pressure and Conditional Flow Structures Downstream of a Reattaching Flow Region," *International Journal of Heat and Fluid Flow*, Vol. 35, June 2012, pp. 119–129. doi:10.1016/j.ijheatfluidflow.2012.04.005

[11] Murray, N. E., and Ukeiley, L. S., "Estimating the Shear Layer Velocity Field Above an Open Cavity from Surface Pressure Measurements," *32nd AIAA Fluid Dynamics Conference and Exhibit*, AIAA, Reston, VA, 2002.

[12] Murray, N. E., and Ukeiley, L. S., "Estimation of the Flow Field from Surface Pressure Measurements in an Open Cavity," *AIAA Journal*, Vol. 41, No. 5, 2003, pp. 969–972. doi:10.2514/2.2035

[13] Murray, N. E., and Ukeiley, L. S., "Modified Quadratic Stochastic Estimation of Resonating Subsonic Cavity Flow," *Journal of Turbulence*, Vol. 8, Dec. 2007, p. N53. doi:10.1080/14685240701656121

[14] Ukeiley, L., and Murray, N., "Velocity and Surface Pressure Measurements in an Open Cavity," *Experiments in Fluids*, Vol. 38, No. 5, 2005, pp. 656–671. doi:10.1007/s00348-005-0948-x

[15] Arunajatesan, C. K., Kannepalli, C., and Ukeiley, L. S., "Three Dimensional Stochastic Estimation Applied to Cavity Flow Fields," *37th AIAA Fluid Dynamics Conference and Exhibit*, AIAA, Reston, VA, 2007.

[16] Ukeiley, L., Murray, N., Song, Q., and Cattafesta, L., "Dynamic Surface Pressure Based Estimation for Flow Control," *IUTAM Symposium on Flow Control and MEMS*, Springer, The Netherlands, 2008, pp. 183–189.

[17] Zhang, K., and Naguib, A. M., "Effect of Finite Cavity Width on Flow Oscillation in a Low-Mach-Number Cavity Flow," *Experiments in fluids*, Vol. 51, No. 5, 2011, pp. 1209–1229. doi:10.1007/s00348-011-1142-y

[18] Lasagna, D., Orazi, M., and Iuso, G., "Multi-Time Delay, Multi Point Linear Stochastic Estimation of a Cavity Shear Layer Velocity from Wall-Pressure Measurements," *Physics of Fluids*, Vol. 25, No. 1, 2013, Paper 017101.

[19] Cole, D. R., Glauser, M. N., and Guezennec, Y. G., "An Application of the Stochastic Estimation to the Jet Mixing Layer," *Physics of Fluids A: Fluid Dynamics*, Vol. 4, No. 1, 1992, pp. 192–194.

[20] Gutmark, E. J., Verfaillie, S., Bonnet, J. P., and Grinstein, F., "Linear Stochastic Estimation of a Swirling Jet," *AIAA Journal*, Vol. 44, No. 3, 2006, pp. 457–468. doi:10.2514/1.19237

[21] Gieseke, T. J., and Guezennec, Y. G., "Stochastic Estimation of Multipoint Conditional Averages and Their Spatio-Temporal Evolution," *Applied Scientific Research*, Vol. 53, No. 3, 1994, pp. 305–320. doi:10.1007/BF00849107

[22] Perrin, R., Braza, M., Cid, E., Cazin, S., Barthet, A., Sevrain, A., and Thiele, F., "Obtaining Phase Averaged Turbulence Properties in the Near Wake of a Circular Cylinder at High Reynolds Number Using POD," *Experiments in Fluids*, Vol. 43, Nos. 2–3, 2007, pp. 341–355. doi:10.1007/s00348-007-0347-6

[23] Durgesh, V., and Naughton, J. W., "Multi-Time-Delay LSE-POD Complementary Approach Applied to Unsteady High-Reynolds-Number near Wake Flow," *Experiments in Fluids*, Vol. 49, No. 3, 2010, pp. 571–583. doi:10.1007/s00348-010-0821-4

[24] Ruiz, T., Sicot, C., Brizzi, L. E., Borée, J., and Gervais, Y., "Pressure/Velocity Coupling Induced by a Near Wall Wake," *Experiments in Fluids*, Vol. 49, No. 1, 2010, pp. 147–165. doi:10.1007/s00348-010-0820-5

[25] Clark, H., Naghib-Lahouti, A., and Lavoie, P., "General Perspectives on Model Construction and Evaluation for Stochastic Estimation, with Application to a Blunt Trailing Edge Wake," *Experiments in Fluids*, Vol. 55, No. 7, 2014, pp. 1–19. doi:10.1007/s00348-014-1756-y

[26] Hosseini, Z., Martinuzzi, R. J., and Noack, B. R., "Sensor-Based Estimation of the Velocity in the Wake of a Low-Aspect-Ratio Pyramid," *Experiments in Fluids*, Vol. 56, No. 1, 2015, pp. 1–16. doi:10.1007/s00348-014-1880-8

[27] Adrian, R. J., "Stochastic Estimation of Conditional Structure: A Review," *Applied Scientific Research*, Vol. 53, No. 3, 1994, pp. 291–303. doi:10.1007/BF00849106

[28] Guezennec, Y. G., "Stochastic Estimation of Coherent Structures in Turbulent Boundary Layers," *Physics of Fluids A: Fluid Dynamics*, Vol. 1, No. 6, 1989, pp. 1054–1060. doi:10.1063/1.857396

[29] Tinney, C. E., Coiffet, F., Delville, J., Hall, A. M., Jordan, P., and Glauser, M. N., "On Spectral Linear Stochastic Estimation," *Experiments in Fluids*, Vol. 41, No. 5, 2006, pp. 763–775. doi:10.1007/s00348-006-0199-5

[30] Caraballo, E., Little, J., Debiasi, M., and Samimy, M., "Development and Implementation of an Experimental-Based Reduced-Order Model for Feedback Control of Subsonic Cavity Flows," *Journal of Fluids Engineering*, Vol. 129, No. 7, 2007, pp. 813–824. doi:10.1115/1.2742724

[31] Kastner, J., Cuppoletti, D., Gutmark, E., Fahrland, A., Jeffries, J., and Hanson, R., "Simultaneous Measurement of Flow Fluctuations and Near-Field Pressure in a Subsonic Jet," *15th AIAA/CEAS Aeroacoustics Conference*, AIAA, Reston, VA, 2009.

[32] O'meara, M., and Mueller, T. J., "Laminar Separation Bubble Characteristics on an Airfoil at Low Reynolds Numbers," *AIAA Journal*, Vol. 25, No. 8, 1987, pp. 1033–1041. doi:10.2514/3.9739

[33] Theofilis, V., Hein, S., and Dallmann, U., "On the Origins of Unsteadiness and Three-Dimensionality in a Laminar Separation Bubble," *Philosophical Transactions of the Royal Society of London A: Mathematical, Physical and Engineering Sciences*, Vol. 358, No. 1777, 2000, pp. 3229–3246. doi:10.1098/rsta.2000.0706

[34] Burgmann, S., Brücker, C., and Schröder, W., "Scanning PIV Measurements of a Laminar Separation Bubble," *Experiments in Fluids*, Vol. 41, No. 2, 2006, pp. 319–326. doi:10.1007/s00348-006-0153-6

[35] Watmuff, J. H., "Evolution of a Wave Packet into Vortex Loops in a Laminar Separation Bubble," *Journal of Fluid Mechanics*, Vol. 397, Oct. 1999, pp. 119–169. doi:10.1017/S0022112099006138

[36] Brinkerhoff, J. R., and Yaras, M. I., "Interaction of Viscous and Inviscid Instability Modes in Separation–Bubble Transition," *Physics of Fluids*, Vol. 23, No. 12, 2011, Paper 124102. doi:10.1063/1.3666844

[37] Kirk, T. M., and Yarusevych, S., "Vortex Shedding Within Laminar Separation Bubbles Forming over an Airfoil," *Experiments in Fluids*, Vol. 58, No. 5, 2017, p. 43. doi:10.1007/s00348-017-2308-z

[38] Lang, M., Rist, U., and Wagner, S., "Investigations on Controlled Transition Development in a Laminar Separation Bubble by Means of LDA and PIV," *Experiments in Fluids*, Vol. 36, No. 1, 2004, pp. 43–52. doi:10.1007/s00348-003-0625-x

[39] Simoni, D., Ubaldi, M., Zunino, P., and Bertini, F., "Transition Mechanisms in Laminar Separation Bubbles with and Without Incoming Wakes and Synthetic Jet Effects," *Experiments in Fluids*, Vol. 53, No. 1, 2012, pp. 173–186. doi:10.1007/s00348-012-1281-9

[40] DeMauro, E. P., Dell'Orso, H., Zaremski, S., Leong, C. M., and Amitay, M., "Control of Laminar Separation Bubble on NACA 0009 Airfoil Using Electroactive Polymers," *AIAA Journal*, Vol. 53, No. 8, 2015, pp. 2270–2279. doi:10.2514/1.J053670

[41] Yarusevych, S., and Kotsonis, M., "Effect of Local DBD Plasma Actuation on Transition in a Laminar Separation Bubble," *Flow, Turbulence and Combustion*, Vol. 98, No. 1, 2017, pp. 195–216. doi:10.1007/s10494-016-9738-1

[42] Yarusevych, S., and Kotsonis, M., "Steady and Transient Response of a Laminar Separation Bubble to Controlled Disturbances," *Journal of Fluid Mechanics*, Vol. 813, Feb. 2017, pp. 955–990. doi:10.1017/jfm.2016.848

[43] Agate, M., Pande, A., Little, J. C., Gross, A., and Fasel, H. F., "Active Flow Control of the Laminar Separation Bubble on an Oscillating Airfoil near Stall," *2018 AIAA Aerospace Sciences Meeting*, AIAA, Reston, VA, 2018.

[44] Garcia-Sagrado, A., and Hynes, T., "Stochastic Estimation of Flow near the Trailing Edge of a NACA0012 Airfoil," *Experiments in Fluids*, Vol. 51, No. 4, 2011, pp. 1057–1071. doi:10.1007/s00348-011-1071-9

[45] Allen, D. M., "Mean Square Error of Prediction as a Criterion for Selecting Variables," *Technometrics*, Vol. 13, No. 3, 1971, pp. 469–475. doi:10.1080/00401706.1971.10488811

[46] Gerakopulos, R., and Yarusevych, S., "Novel Time-Resolved Pressure Measurements on an Airfoil at a Low Reynolds Number," *AIAA Journal*, Vol. 50, No. 5, 2012, pp. 1189–1200. doi:10.2514/1.J051472

[47] Westerweel, J., and Scarano, F., "Universal Outlier Detection for PIV Data," *Experiments in Fluids*, Vol. 39, No. 6, 2005, pp. 1096–1100. doi:10.1007/s00348-005-0016-6

[48] Weineke, B., "PIV Uncertainty Quantification from Correlation Statistics," *Experiments in Fluids*, Vol. 26, No. 7, 2015, Paper 074002.

[49] Kurelek, J., and Yarusevych, S. V., "The Effect of Acoustic Excitation on the Later Stages of Transition in a Laminar Separation Bubble," *46th AIAA Fluid Dynamics Conference*, AIAA Paper 2016-3948, 2016.

[50] Kurelek, J., Tuna, B. A., and Yarusevych, S. V., "Three-Dimensional Vortex Development in a Laminar Separation Bubble Formed over an Airfoil," *47th AIAA Fluid Dynamics Conference*, AIAA Paper 2017-3642, 2017.

[51] Fitzgerald, E. J., and Mueller, T. J., "Measurements in a Separation Bubble on an Airfoil Using Laser Velocimetry," *AIAA Journal*, Vol. 28, No. 4, 1990, pp. 584–592. doi:10.2514/3.10433

[52] Doligalski, T. L., Smith, C. R., and Walker, J. D. A., "Vortex Interactions with Walls," *Annual Review of Fluid Mechanics*, Vol. 26, No. 1, 1994, pp. 573–616. doi:10.1146/annurev.fl.26.010194.003041

[53] Lang, M., Rist, U., and Wagner, S., "Investigations on Controlled Transition Development in a Laminar Separation Bubble by Means of LDA and PIV," *Experiments in Fluids*, Vol. 36, No. 1, 2004, pp. 43–52. doi:10.1007/s00348-003-0625-x

[54] Boutilier, M. S., and Yarusevych, S., "Separated Shear Layer Transition over an Airfoil at a Low Reynolds Number," *Physics of Fluids*, Vol. 24, No. 8, 2012, Paper 084105. doi:10.1063/1.4744989

[55] Jeong, J., and Hussain, F., "On the Identification of a Vortex," *Journal of Fluid Mechanics*, Vol. 285, Feb. 1995, pp. 69–94. doi:10.1017/S0022112095000462

[56] Graftieaux, L., Michard, M., and Grosjean, N., "Combining PIV, POD and Vortex Identification Algorithms for the Study of Unsteady Turbulent Swirling Flows," *Measurement Science and Technology*, Vol. 12, No. 9, 2001, pp. 1422–1429. doi:10.1088/0957-0233/12/9/307

M. Green
Associate Editor